Title
Tunable Second Harmonic Generation in Twisted Bilayer Graphene

Journal
Matter, 3(4)

ISSN
2590-2393

Authors
Yang, Fuyi
Song, Wenshen
Meng, Fanhao
et al.

Publication Date
2020-10-01

DOI
10.1016/j.matt.2020.08.018

Peer reviewed

Tunable Second Harmonic Generation in twisted bilayer graphene

Fuyi Yang[1,2], Wenshen Song[3], Fanhao Meng[1], Fuchuan Luo[1,5], Shuai Lou[1,2], Shuren Lin[1,2], Zilun Gong[1], Jinhua Cao[1,2], Edward Bernard[6], Emory Chan[6], Li Yang[3,4], Jie Yao[1,2,7]*

1. Department of Materials Science and Engineering, University of California Berkeley, Berkeley, CA 94720, USA

2. Materials Sciences Division, Lawrence Berkeley National Laboratory, Berkeley, CA 94720, USA

3. Department of Physics, Washington University in St. Louis, St. Louis, MO 63130, USA.

4. Institute of Materials Science and Engineering, Washington University in St. Louis, St. Louis, MO 63130, USA.

5. National Engineering Center of Electromagnetic Radiation Control Materials, University of Electronic Science and Technology of China, Chengdu, Jiangsu 610054, RP China

6. The Molecular Foundry, Lawrence Berkeley National Laboratory, Berkeley, CA, 94720, USA

7. Lead Contact

*Correspondence: yaojie@berkeley.edu

SUMMARY:

Twisted stacking of van der Waals (vdW) materials introduces a new way in bandstructure engineering and has given rise to numerous extraordinary physical phenomena. Despite the absence of second harmonic generation (SHG) in non-gated monolayer graphene, artificially twisted bilayer graphene (tBLG) possesses more possible point-group symmetries including those with broken inversion-symmetry. Here, we report twist-angle-dependent SHG from tBLG, which is the first demonstration of an elemental material with intrinsically tunable nonlinearity. We show that depending on the twist angle, the susceptibility of the dominant chiral tensor component of tBLGs can vary from 0 to 28×10^4 pm^2/V, which is at the same order of magnitude as on-resonance susceptibility of monolayer MoS_2. These results shed light on the underlying symmetry of tBLG systems and electronic band-structure near van Hove singularities (vHs). More importantly, they introduce a new degree of freedom, the twisting, in creating efficient second-order nonlinear material form centrosymmetric constituents.

KEYWORDS:

Twisted bilayer graphene, Second harmonic generation, Chirality, Resonant enhancement.

INTRODUCTION:

The relative twist angle between two adjacent vdW layers has enabled a new degree of freedom in controlling of low dimensional van der Waals (vdW) materials' properties. Recent discoveries of superconductivity, correlated states and emergent ferromagnetism at the 'magic' twist angle revealed the strong interlayer coupling in twisted bilayer graphene (tBLG) systems[1-5]. Flattened bands with a high density of states, often denoted as van Hove singularities (vHs) or anti-crossings, are created in tBLGs when two Dirac cones from each individual layer intersect in momentum space[6]. Scanning tunneling spectroscopy (STS) has shown the twist-angle-dependent vHs by bringing it close to Fermi energy (E_F) through electronic gating[7]. Near these vHs, resonant optical effects, such as enhanced absorption, laser-wavelength dependent Raman, two-photon emission, and strong circular dichroism (CD), have been reported[8-12]. Recently, the excitonic nature of flattened bands in tBLG have also been demonstrated via the exploration of the dynamics of carrier relaxation under one-photon or two-photon resonant photoluminescence excitation (PLE) conditions and multiple transitions with different selection rules have been revealed[9].

The twisting degree of freedom not only allows strength tuning for bandstructure engineering but also the overall symmetry of the system[5], which plays a critical role in various physical processes, including second harmonic generation (SHG). As is well-known, SHG is very sensitive to the symmetry of a material and has been widely accepted as a noninvasive tool for characterizing crystalline orientation and electronic structures[13]. Monolayers of many two-dimensional (2D) van der Waals materials such as hBN, MoS_2 and naturally stacked trilayer graphene have well defined D_{3h} symmetry without an inversion center, and SHG measurements from these materials

have been reported[14, 15]. There are also reports on the SHG from centrosymmetric monolayer graphene due to surface dipole and bulk quadrupole contributions, but these effects are usually weak[16]. SHG generation form centrosymmetric material such as naturally stacked bilayer graphene[17-19] and 2H stacked MoS_2 have been proposed and shown by applying in- or out-of-plane electric field which breaks the inversion symmetry of the system. Although the electric control has its own advantage, the tuning range is usually limited by finite gating voltage and it is difficult to measure those processes[17-19] experimentally due to the low working frequencies. For the observation of strong electric-dipole-enabled SHG, inversion symmetry breaking of the crystal structure and a larger scale of resonant energy are necessary[20]. The twisting we introduced here provides an alternative way to break the inversion symmetry of centrosymmetric materials with larger tuning range and can be further combined with electrical control.

In this work, we report the first experimental observation of tunable SHG in tBLGs with different twisting angles. The tunability is closely related to the change of intrinsic nonlinear dispersion of tBLGs. Moreover, due to the involvement of higher-order tensor in the nonlinear optical process, SHG measurement can unravel more underlying symmetry properties of the tBLG system compared to CD and other linear characterization means. Intuitively, stacking two layers of centrosymmetric materials would not give rise to strong SHG with only surface interactions. Due to the breaking inversion symmetry and strong interlayer couplings resulting from the twist in tBLG systems, SHG comes from the entire two-layer material instead of the interface. As shown schematically in Figure 1a, naturally stacked bilayer graphene remains centrosymmetric whether they are any kinds of translational displacement (T). This is not true, however, if a relative twist angle other than 0° or multiples of 60° is introduced by a rotational

operation (R). It can be mathematically proven that: if we invert the top graphene layer through an arbitrary point in the middle plane, it cannot overlap with the bottom layer (Figure S17). Therefore, the bilayer structure lacks the inversion symmetry which is the case for tBLGs. The above proof and the strong interlayer coupling in tBLG systems which is manifested as vHs in the density of electronic states of the system, allows SHG to be generated from the entire two-layer material instead of the interface. In addition, the transition between vHs points in the valance and conduction bands (E_{vHs}) can further contribute to SHG enhancement when incident photons fulfill 1- or 2- photon resonant SHG conditions (Figure 1c), giving rise to a twist-angle dependent SHG response. Therefore, the mechanism for SHG demonstrated in this work is enabled by the hybridized electronic states engineered by the twisting degree of freedom and the mechanism is different form the twisted transition metal dichalcogenide (TMDC) systems. Since TMDC itself is non-centrosymmetric, varied SHG emissions from layered TMDC are due to SHG interference between single layers. On the other hand, in tBLG, constituting graphene is centrosymmetric and the SHG comes from inversion symmetry breaking in the hybrid graphene layers. More specifically, in layered TMDC, SHG efficiency changes with twist angle due to different interference conditions[21, 22] (constructive, destructive or partially constructive) instead of different degree of hybridization between layers. In tBLG, however, the twist completely changes the symmetry of the materials and the efficiency is determined by the underlying hybrid electronic structure. Therefore, it is more sensitive to the twisting compared to TMDC and shows pronounced enhancement when the incident energy matches E_{vHs} as shown below.

RESULTS AND DISCUSSIONS:

Raman and SHG characterization of tBLG samples

TBLG samples were prepared by a dry transfer method, with which different twisting angles can be realized. Before picking up the upmost hBN layer using polypropylene carbonate (PPC) stamp, we conducted SHG mapping on the exfoliated hBN nanosheets to ensure that they are uniform and even-layered, which excludes possible contributions from hBN in the final SHG results. To further avoid strain-induced effects at the interface from bubbles between hBN and the first layer of graphene, we adopted the recently published method[23] by stacking hBN onto graphene at a high temperature, which resulted in a relatively clean surface in the twisted region like the one shown in Figure 1d. It can also be readily identified under the optical microscope (highlighted with the red box). The angles of the sample were verified by Raman measurements under 532nm excitation (Figure S1a). The linear absorption measurements give the same estimation of the twist angle (Figure S18). Comparison of Raman spectra of the tBLG and single-layer graphene for the sample in Figure 1d is plotted in Figure 2a. The peak around 1366 cm^{-1} is attributed to hBN. The R peak showing up on higher wavenumber side of the G peak at 1627 cm^{-1} is usually associated with the intervalley double-resonance process in tBLG systems[10] and corresponds to the twist angle around 8° in this case. Figure 1e shows the integrated intensity of the Raman R peak across the whole sample. The sharp contrast between the twisted and untwisted regions is clear, matching those in the optical image. More Raman maps can be found in the Figure S2 and S3.

Figure 1f shows the SHG mapping of the same area by exciting the sample with a continuous wave (CW) laser at the wavelength of 1064nm under normal incidence with collection signal around 532nm. From the mapping results, we can clearly identify a strong emission in the tBLG region and its second-order nature is confirmed by the power-dependent measurement plotted in

Figure 2b. SHG spectra of tBLG with 6° twist angle, trilayer graphene (TLG), and CVD grown monolayer MoS_2 are shown in Figure 2c. The inset compares the SHG efficiency of these three materials under the same conditions and SHG from tBLG is comparable to monolayer MoS_2 at this wavelength. Based on the vector model[24], we calibrated the nonlinear susceptibility of 6° twist angle to be around $28 \times 10^4\ pm^2/V$ under resonant excitation condition, which is comparable to the on-resonant susceptibility of monolayer MoS_2[14, 25, 26] (Details of calibration can be found in Experimental Procedure section). Another notable feature is that the SHG spectrum of tBLG has only one sharp peak centered around 532nm without any broadband nonlinear photoluminescence, which is contrary to the case when the excitation and relaxation processes are on the femtosecond scale[27-29]. Although there are theoretical predictions on the emergence of SHG in graphene/hBN system due to sublattice asymmetry in the graphene layer[17], it cannot account for the results we observed here. For those regions which consist of monolayer graphene and hBN (highlighted with the green box in Figure 1e), there are no detectable SHG signals. The fact that we did not observe any SHG signal from pure graphene layer on SiO_2/Si substrate (highlighted with the blue box in Figure 1e) also rules out the possibility that the observed SHG signal arises from the breaking of inversion symmetry of graphene by the presence of the oxidized silicon substrate[16].

Second harmonic generation (SHG) is known to occur due to an atomic response that scales quadratically with the strength of the incident optical field. The induced polarization at the SHG frequency is usually written as $P_i(2\omega) = \chi^{(2)}_{ijk}(2\omega;\omega,\omega)E_j(\omega)E_k(\omega)$, where $\chi^{(2)}_{ijk}(2\omega;\omega,\omega)$ is the second-order susceptibility which is a third-order tensor relating the vectorial incident field at frequency ω to the induced polarization at doubled frequency 2ω. Non-zero components in

$\chi_{ijk}^{(2)}(2\omega;\omega,\omega)$ can usually be reduced and determined by considering the space group of the crystalline medium[20]. As such, the SHG signal is very sensitive to the underlying symmetry of the materials and we explored the contributions from different components using the SHG polarization method[20]. Although the inversion symmetry is broken in tBLG samples, the exact point-group symmetry cannot be accurately defined because of different choices of the twisting center[5, 30]. For example, at a specific commensurate twist angle, the point-group symmetry of tBLG is either D_3 or D_6 depending on whether the twisting center is carbon atom or hexagonal center. In addition, the symmetry will reduce to C_3 or C_6 if the angles become incommensurate[5, 30]. However, it has been reported that the exact symmetry of tBLG may only affect the electronic behavior of the system on the scale of meV. The susceptibility calculations shown below also suggests that it is the universal chirality instead of the exact symmetry of tBLG system that determines the ultimate SHG response.

Closer investigation on the second-order susceptibility of tBLG with different point-symmetry shows that it is always possible to find a non-zero tensor component χ_{xyz} associated with the chirality[31, 32]. Moreover, the resonant and dispersive behavior of tBLG in the visible range due to the semimetal and anticrossed band structure point towards the failure of Kleinman symmetry in describing the second-order susceptibility[33]. Thus, the contribution from the chiral tensor component χ_{xyz} cannot be neglected here and this prediction agrees with both DFT simulations[34] and our SHG polarization measurements as shown below.

SHG polarization measurements

We use linearly polarized excitation at λ=1064nm with normal incidence through an objective lens with a numerical aperture NA=0.9. We rotated the sample with respect to the laser axis and collected reflected SHG signal using the cross-polarization configuration (Details of experimental setup can be found in the Experimental Procedure section). The six-fold symmetric pattern from an odd-layer of hBN (Figure 3a) is representative of a D_{3h} system, and the signal is determined by only one independent tensor component: $I_v \propto \left|\chi_{yyy} \sin(3\theta)\right|^2$, which is consistent with previous reports[14]. However, tBLG samples do not yield same results under the same experimental configuration. As shown in Figure 3b, 3c, and 3d with 8°, 10°, and 12° twist angles respectively, the twist angles are determined by the frequency of Raman R peak before SHG measurements. A clear threefold symmetry can be identified in all tBLG samples. From DFT calculations of a commensurate tBLG model with different twisting centers, we find that the SHG process is dominated by a nearly constant χ_{xyz} independent of the centers (Details of DFT simulation can be found in Experimental Procedure section). In Figure 3e-3f, we plot all in-plane tensor components of a 21.8° tBLG with the carbon atom being the twisting center (DFT calculations of a 13.2° commensurate angle tBLG can be found in Figure S16). The 21.8° commensurate angle is chosen because of the computational efficiency and the space group is C_3 for this specific translational configuration[10, 11]. Thus, due to symmetry reasons, the spectral response of $|\chi_{xyz}|$ ($|\chi_{xyy}|$) is the same as $|\chi_{yxz}|$ ($|\chi_{yxy}|$) with other in-plane tensor elements being negligible. More spectral responses of second-order tensors with different twisting centers can be found in Figure S4 – 7. It can be seen that the non-chiral tensors also contribute and evolve with the interlayer shift except for the AA-like stacking case. However, they show a weak dependence on the twisting center overall[30]. Therefore, we can fit the polarization results with the dominant χ_{xyz} component and the next non-vanishing one, χ_{xxx}. Fitting curves are shown in

Figure 3b-3d and Figure S8, which agrees well with the experimental results (Details of fitting can be found in Experimental Procedure section). Owing to the high NA of the objective lens used, there will always be a finite portion of z polarized light illuminated on the sample and be converted to in-plane polarized SHG field via the χ_{xyz} component[35-37]. By reducing the NA, the proportion of z-polarized field is also diminished resulting in a more drastic decrease of SHG efficiency of tBLGs compared to MoS_2 (Comparisons can be found in Supplementary Table 1).

Resonantly enhanced SHG response

Previous works have demonstrated the strong enhancement of G and R band intensity when the energy of laser matches those E_{vHs} in tBLG. By sweeping the incident wavelength and fixing the twisting angle, a clear trend can be obtained by fitting with second or third-order time-dependent perturbation theory[38]. In order to demonstrate the tunable nonlinear response of the tBLG system, here we choose the reverse process, that is, fixing the incident wavelength and sweeping the twist angle, which also give a similar trend due to the resonance matching mechanism. As shown in Figure 4a, when we change tBLG samples while keeping the incident wavelength constant (532nm), the Raman G peak shows pronounced enhancement when E_{vHs}=2.23eV with twist angle to be around 12°, which is consistent with other reports when incident wavelength is swept[10, 39] (Details of fitting can be found in Experimental Procedure section).

We collected the SHG at 392.5nm from all tBLG samples with different twist angle while keeping the incident wavelength at 785nm (The results of angle sweeping with 1064nm laser can be found in the Figure S9). High efficiency of SHG is observed when the E_{vHs} is around 1.58eV and 3.16eV as shown in Figure 4b with the corresponding twist angles to be about 8° and 20°

respectively[10, 39]. Such a dependence of SHG intensity on varying vHs levels indicates resonant SHG processes[40, 41], where the SHG is enhanced when one or two incident photons are in resonance with electronic transitions in tBLG. Note that the dependence of E_{vHs} on twist angle does not follow the relation $E_{vHs}=3.9\sin(3\theta)$ exactly, especially at large twist angles (More information can be found in Figure S1b). For the resonant transitions involved in the SHG process, we use a coherent superposition of second-order nonlinear susceptibility of 1- and 2-photon resonances[42, 43] and the theory fits the experimental data very well (solid line in Figure 4b). (Details of fitting can be found in Experimental Procedure section) Considering the computational difficulty to calculate the susceptibility of tBLG with small twist angles[10, 11], we compare the imaginary part of linear permittivity in the z-direction with the dominant tensor component, χ_{xyz}, of a 21.8° tBLG in Figure 4c. $\varepsilon_{zz}(\omega)$ shows a dominate peak around E_{vHs} for a 21.8° tBLG. Although decaying in the low-frequency range, it is still finite at halved E_{vHs}. Besides, the involvement of dipolar response in z-direction validates the non-vanishing χ_{xyz} and the spectral overlap supports both resonant processes. The static SH signal clearly shows the 1- and 2-photon resonant enhancement when the incident energy matches with electronic transitions. When there is significant absorption in tBLG, the magnitude of second-order susceptibility might be affected by the photoexcitation and the rising lattice temperature[50-52], although these factors do not change the basic mechanism for the SHG process in tBLG. More dedicated experiments, for example time-resolved measurement will provide a better understanding of the influence of electronic dynamics on the nonlinear response in tBLG system. The novel and tunable low dimensional nonlinear material demonstrated here can be readily integrated onto silicon waveguides and resonators for integrated nonlinear optics applications. The large χ_{xyz} not only allows the strong interaction with usually unaccessible TM modes, but also enables more

efficient phase matching of the nonlinear process. More advanced control such as gating in tuning the nonlinear behavior of tBLG can further deepen our understanding of the material system as well as enlarge the working bandwidth of integrated nonlinear platform.

CONCLUSIONS:

In summary, we observed the twist-angle-dependent SHG in inversion-symmetry-broken tBLGs. The extracted susceptibility of on-resonant tBLG is comparable to on-resonant monolayer MoS_2 and remains non-vanishing over a range of angles. The tunable SHG achieved here differs from previous nonlinear engineering work that based on the fixed susceptibility dispersion[41]. Enabled by tBLG system, determinant factors of SHG response such as underlying symmetry and electronic structure can be readily changed just by twisting. Conventional approaches are limited in uncovering the symmetry elements of the tBLG system. Linear optical and Raman responses of tBLG are isotropic and cannot be used to tell the high symmetry axes of the system. Scanning Tunneling Microscopy (SEM), Transmission Electron Microscopy (TEM) and Electron Diffraction are the common methods to characterize the stacking configuration of tBLG samples. With combined contributions of dominant chiral tensor component, χ_{xyz} and other non-chiral ones, the SHG measurement of tBLG will give rise to polarization patterns with 3-fold symmetry which potentially allow an easier identification of the high symmetry axes in tBLG samples compared to previously mentioned methods. The same strategy can be applied to the material with similar symmetry. The involvement of the z-polarized field and the large magnitude of χ_{xyz} we found here provide a new perspective to explore the exciton levels around vHs transition frequency. Moreover, the existence of χ_{xyz} unravels the possible piezoelectric properties which may motivate further mechanical studies on tBLG systems. Due to the strong interlayer coupling

between artificially stacked graphene, we also expect exotic nonlinear behavior from multi-layer stacked graphene and other vdW materials with more complicated crystal symmetries[11, 44].

EXPERIMENTAL PROCEDURES

Resource Availability

Lead Contact

Jie Yao serves as the lead contact (yaojie@berkeley.edu).

Materials Availability

No new reagents were generated in this study.

Data and Code Availability

All data are available upon reasonable request.

DFT and SHG simulation details

For simulations, a commensuration cell[45] consists of 28 C atoms is built by twisting upper layer of AB stacking bilayer graphene by $21.79°$, with the axis on one C atom having no corresponding C atom at the other layer. First-principles calculations are implemented in the Vienna ab initio simulation package (VASP)[46, 47] to obtain relaxed atomistic structures and electronic structures, based on density functional theory (DFT) within the generalized gradient approximation using the Perdew-Burke-Ernzerhof (GGA-PBE) functional[48]. The plane-wave energy cutoff is set to be 400 eV. The van der Waals (vdW) interaction is included through the DFT-D2 method of Grimme[49]. For linear and nonlinear optics calculation, we use a dense $26 \times 26 \times 1$ k-grid sampling in reciprocal space and 80 total electronic bands to guarantee converged results. Linear permittivity and second harmonic generation (SHG) are calculated by NLOPACK package[34].

Sample preparation

Single layer graphene and few layer hBN are exfoliated on 300nm SiO_2/Si substrate using the Scotch tape. Before the transfer process we use SHG measurement to determine whether the exfoliated hBNs are even-layer or odd-layer. Only the even-layer ones are used in the transfer and sample preparation processes. PPC/PDMS stamps are prepared following the reported method[23]. By attaching the stamp on a vertical stage and the substrate on a rotatable mount, we are able to pick up hBN and use this hBN to pick up one half of the graphene layer. By rotating the mount with another half of graphene layer on it to the desired angle and align it with the previous half on the stamp, a tBLG sample can be made.

Optical measurements

SHG mapping and polarization measurement setup is shown in Figure S10. Excitation beam from a CW laser is first sent through a linear polarizer (LP) orientated in X direction and then focused on to the sample by a high-NA objective lens. TBLG samples are mounted on an XY Piezo Stage to achieve spatial SHG resolution. Emission from the sample is first collimated by the objective lens, then filtered by a short pass filter (SP) to get rid of excitation beam. Finally, the SHG emission is focused onto the silt of the spectrometer with silicon detector by a detector lens (L). For polarization measurement, another polarizer is placed perpendicular to the excitation polarization (Y direction) before the detector lens and the sample is rotated around the sample normal. The setup for Raman measurement is similar to the SHG except that the laser has a wavelength at 532nm (CW) and the SP is replaced by a 532nm Raman filter.

One of the CW laser Model we used in this work is Ventus 1064 (Laser Quantum) and the maximum power output is 100mW. The power after the objective lens is measured to be 90mW and the focused light spot is ~ 4.5um. The second CW laser system we used is Littman/Metcalf 785nm (Sacher Lasertechnik) with output power 100mW and focused light spot is ~ 4um.

Nonlinear susceptibility calibration of tBLG

The general relation between second-order polarization and incident electric field is:

$$\begin{bmatrix} P_x(2\omega) \\ P_y(2\omega) \\ P_z(2\omega) \end{bmatrix} = \epsilon_0 \begin{bmatrix} \chi_{xxx} & \chi_{xyy} & \chi_{xzz} & \chi_{xyz} & \chi_{xzx} & \chi_{xxy} \\ \chi_{yxx} & \chi_{yyy} & \chi_{yzz} & \chi_{yyz} & \chi_{yzx} & \chi_{yzz} \\ \chi_{zxx} & \chi_{zyy} & \chi_{zzz} & \chi_{zyz} & \chi_{zzx} & \chi_{zzz} \end{bmatrix} \begin{bmatrix} E_x^2(\omega) \\ E_y^2(\omega) \\ E_z^2(\omega) \\ 2E_y(\omega)E_z(\omega) \\ 2E_x(\omega)E_z(\omega) \\ 2E_x(\omega)E_y(\omega) \end{bmatrix}$$

For monolayer MoS_2 with D_{3h} symmetry, the SH susceptibility reduces to the following form with only one independent tensor component:

$$\begin{bmatrix} \chi_{xxx} & -\chi_{xxx} & 0 & 0 & 0 & 0 \\ 0 & 0 & 0 & 0 & 0 & -\chi_{xxx} \\ 0 & 0 & 0 & 0 & 0 & 0 \end{bmatrix}$$

Therefore, for MoS_2 the detected SH signal without any polarizer before the detector (LP Y) is:

$$I_{MoS_2}(2\omega) = C\chi_{xxx}^2 I(\omega)^2,$$

where C is a proportionality constant determined by the local dielectric environment[25] and $I(\omega)$ is the intensity of incident fundamental field. For tBLG we can reduce the tensor matrix according to C_3 crystal symmetry and there are 8 independent elements left:

$$\begin{bmatrix} \chi_{xxx} & -\chi_{xxx} & 0 & \chi_{xyz} & \chi_{xzx} & -\chi_{yyy} \\ -\chi_{yyy} & \chi_{yyy} & 0 & \chi_{yyz} & -\chi_{xyz} & -\chi_{xxx} \\ \chi_{zxx} & \chi_{zxx} & \chi_{zzz} & 0 & 0 & 0 \end{bmatrix}$$

Based on our SHG DFT simulation resultsonly χ_{xyz} and χ_{xxx} are nonzero for C_3 symmetry (Figure S1e and S1f). Assuming the same incident and local environment condition as MoS_2, which is valid in our experiment, the SHG from tBLG is:

$$I_{tBLG}(2\omega) = C(\chi_{xxx}^2 + 4f^2\chi_{xyz}^2 - 4\mathrm{f}\chi_{xxx}\chi_{xyz}\sin(3\theta))\, I(\omega)^2,$$

The DFT results for both 21.8° and 13.2° tBLGs show that χ_{xxx} is much smaller than χ_{xyz}. Thus, we can use $I_{tBLG}(2\omega) = C(4f^2\chi_{xyz}^2)I(\omega)^2$ to get a lower bound for the estimation of tBLG susceptibility. Here *f* is the ratio of how much z-polarized light is converted by the high NA objective lens.

Due to the vectorial nature of light-matter interaction in the second order, the field distribution in the focal volume of a high-NA objective cannot be described by paraxial approximation anymore and the longitudinal component of polarization are nonnegligible[35, 36]. Therefore, we adopt the vectorial Debye diffraction theory here to analyze the field distribution of fundamental light at focal plane and estimate the value of *f* in the above expression.

As schematically shown Figure S11a, the illuminating part of SHG measurement consists of a high NA objective lens and we will only consider linearly polarized fundamental field (X polarized) for further discussion. Based on the integral formula from Richard and Wolf[24], when incident light is polarized in X direction by an infinity-corrected objective, the electric field at focal plane can be expressed as:

$$E_x(\boldsymbol{r}) = -i[I_0 + I_2\cos(2\varphi)]$$

$$E_y(\boldsymbol{r}) = -iI_2\sin(2\varphi)$$

$$E_z(\boldsymbol{r}) = -I_1\cos(\varphi)$$

And the integrals I_n are defined as:

$$I_0 = \int_0^{\alpha} \cos(\theta)^{1/2}\sin(\theta)(1+\cos(\theta))J_0(krsin(\theta))\exp(ikzcos(\theta))d\theta$$

$$I_1 = \int_0^{\alpha} \cos(\theta)^{1/2}\sin(\theta)^2 J_1(krsin(\theta))\exp(ikzcos(\theta))d\theta$$

$$I_2 = \int_0^{\alpha} \cos(\theta)^{1/2}\sin(\theta)(1-\cos(\theta))J_2(krsin(\theta))\exp(ikzcos(\theta))d\theta$$

Where φ is the azimuthal and of point **r** in the focal plane, θ characterizes the incident angle which spans form 0 to α, the maximal angle determined by the NA of illumination objective ($\alpha = \sin(NA/n)^{-1}$).

Figure S11b shows the peak intensity and field ratio of the longitudinal Z component versus transverse X component at the focal plane as a function of NA for 1064nm incident light. The Y-polarized component is neglected due to its extremely small value. For the specific objective len we used (NA=0.9), E_z/E_x, i.e., f value, is about 0.1∼0.2 which is consistent with previous calculations[35]. Moreover, the ability to efficiently collect the emission from dark excitons in TMDC using high NA objective (NA=0.82) has been experimentally achieved[37], where the authors estimates the percentage of z-polarized component to be around 9%, and agrees with our result.

By adding analyzer vertical or parallel to the incident laser polarization and rotate the sample around the laser axis, we can find that the SHG polarization pattern of tBLG satisfies following expression, respectively:

$$I_{vertical}(\theta) \propto (2f\chi_{xyz} + \chi_{xxx}\sin(3\theta))^2$$

$$I_{parallel}(\theta) \propto \chi_{xxx}^2 \cos(\theta)^2 (1-2\sin(2\theta))^2$$

Here, we take f to be 0.1 following above analysis and fit the experimental vertical polarization results with $I_{vertical}(\theta)$. We find that only when χ_{xyz} is much larger than χ_{xxx}, a good fit can be

attained. Considering the fact that χ_{xxx} is a small value, $I_{parallel}$ becomes almost two orders of magnitude smaller than $I_{vertical}$ and the SHG signal with a parallel analyzer falls below the detection limit of our system during measurement. Therefore, we are not able to fit parallel polarization results and obtain more quantitative estimations of the value of χ_{xyz} and χ_{xxx}. Figure S8 shows polarization result with two kinds of the analyzer for an odd-layer hBN and a tBLG sample.

To further reveal the field distribution of X-polarized incident field focused by a high NA objective (NA=0.9), we plot the magnitude and phase of E_x and E_z at focal plane in Figure S12 based on the same integral formula. As we can see in Figure S12a and S12c, E_x is rotationally symmetrical and is in phase in the region of interest while the magnitude peaks of E_z locate at the X axis and are out of phase (Figure S11b and S11d). It is the overlap between E_x and E_z field that is responsible for the SH response through χ_{xyz}. Although one might think that the SHG contributed from out-of-phase E_z field will cancel each other in the far field intuitively, we will show that this is not the case by taking into account the phase factor in vectorical Debye theory when simulating the SHG collection process in the followings.

Since the SHG process of MoS_2 has been well studied and calibrated[14, 25, 26], it serves as an excellent reference to calibrate the nonlinear susceptibility of the tBLG. Having the estimation of *f*, we can calculate the susceptibility of tBLG and trilayer graphene based on measured data. Consider trilayer graphene (TLG), 6° tBLG, and monolayer MoS_2 SHG measurements under the same conditions (same 1064nm CW laser, excitation power, optical setup, laser focus, substrate) and the SH signal without any analyzer is shown in Figure 2c. Since TLG has the same symmetry as MoS_2, the equation governs SHG efficiency would also be the same with only one independent tensor for both systems. Therefore $\frac{\chi_{xxx,TLG}}{\chi_{xxx,MoS_2}} = \sqrt{\frac{I(2\omega)_{TLG}}{I(2\omega)_{MoS_2}}}$. Following the above

analysis for tBLG, we get $\frac{\chi_{xyz,tBLG}}{\chi_{xxx,MoS_2}} = \frac{1}{2f}\sqrt{\frac{I(2\omega)_{tBLG}}{I(2\omega)_{MoS_2}}}$. Taking the SH susceptibility of MoS_2 around 1064nm from theoretical and experimental work which is ~0.7 (10^4 pm^2/V), we get $\chi_{xxx,TLG}$ is about 0.49 (10^4 pm^2/V) and $\chi_{xyz,tBLG}$ is approximately 1.7 ~ 3.3 (10^4 pm^2/V). It can be seen that the susceptibility of on-resonance tBLG is higher than off-resonant MoS_2, but generally on the same order of 10^4 pm^2/V. To further confirm our evaluation, the results from DFT calculation are shown in Figure 3f-3e for 21.8° commensurate angle tBLG. At resonance, χ_{xyz} is indeed on the same order of the result from experimental data.

The above evaluation of nonlinear susceptibility for tBLG is actually overly underestimated due to the ignorance of χ_{xxx} and the fact that E_z field only has finite overlap with E_x in the focal region. In order to get a more accurate estimation of χ_{xyz} for the 6° tBLG under resonant excitation, we simulate the evolution of SH signal through the detecting system with spatially varying E_x and E_z in the framework of vectorical Debye diffraction model. The detecting system of SH signal is shown in Figure S13 with the same objective lens as in the illuminating system (Figure S11).

In the simulation, the induced second-order polarization in tBLG sample can be taken as a two-dimensional collection of dipoles, of which the directions are determined by the nonlinear tensors. The far-field radiation can be calculated as the superposition of all these dipoles:

$$E_{dipoles} = \frac{e^{2ikR}}{4\pi R}\int e^{-2ik\boldsymbol{s}\cdot\boldsymbol{r}}\{\boldsymbol{s}\times[\boldsymbol{s}\times\boldsymbol{P}(\boldsymbol{r})]\}dr^2$$

Where $\boldsymbol{P}(\boldsymbol{r})$ is the induced SH polarization, $E_{dipoles}$ is the radiated SH field, R is the observation point at plane $\boldsymbol{E_1}$ behind the objective, r is the coordinate in the focal plane and s is the unit vector in the observation direction.

Following the standard method[24], the electric vectors ($\boldsymbol{E_1}$) of SH signal behind the collimating objective is:

$$E_{1x} = \cos(\theta)^{-\frac{1}{2}}(-a_1 B_x - a_2 B_y + a_3 B_z)$$

$$E_{1y} = \cos(\theta)^{-\frac{1}{2}}(-a_2 B_x - a_4 B_y + a_5 B_z)$$

$$E_{1z} = 0$$

Where

$a_1 = \sin(\varphi)^2 + \emptyset \cos(\varphi)^2 \cos(\theta)$

$a_2 = \sin(\varphi)\cos(\varphi)(\cos(\theta) - 1)$

$a_3 = \cos(\varphi)\sin(\theta)$

$a_4 = \sin(\varphi)^2 \cos(\theta) + \cos(\varphi)^2$

$a_5 = \sin(\varphi)\sin(\theta)$

$$B_x = \frac{e^{2ik_2R}}{4\pi R}\int e^{-2ik_2 s\cdot r} P_x dr^2$$

$$B_y = \frac{e^{2ik_2R}}{4\pi R}\int e^{-2ik_2 s\cdot r} P_y dr^2$$

$$B_z = \frac{e^{2ik_2R}}{4\pi R}\int e^{-2ik_2 s\cdot r} P_z dr^2$$

Here, θ and φ are polar and azimuthal angles of the observation point R as shown in Figure S13, k_2 in the integral is now the wavevector of SH field at doubled frequency of the fundamental wave. In the paraxial approximation, we usually assume emitted SH field vectors to be linearly proportional to the induced SH polarization vectors. However, as we can see in the above expressions, cross-effect between lateral and longitudinal components are possible in the presence of a high-NA objective. In our case, the induced Z-polarized second-order polarization

($\chi_{z..}$) is negligible according to the DFT results (Figure S7), and we only need to consider the collection of induced P_x and P_y.

Behind the objective, another Y-orientated linear polarizer (perpendicular to the incident polarization) is placed before the detecting lens to select cross-polarized SH field. The final detector lens with low NA is used for focusing SH signal to the detector. The collected SH power, therefore, can be calculated by integrating SH field intensity over a spherical surface of radius R within the cone angle of the collimating objective:

$$I = \int_0^{\alpha} d\theta \int_0^{2\pi} d\varphi |\boldsymbol{E}_2(\boldsymbol{R})|^2 \boldsymbol{R}^2 \sin(\theta)$$

For SHG intensity simulations of MoS_2 and tBLG, we apply the same incident field, which is the same field distribution enabled by an objective with 0.9 NA as calculated in Figure S12. We keep incident light to be polarized in X direction and rotate the sample around the sample normal. The angle between X direction in lab frame and x direction in local fame of sample is β.

For MoS_2, the induced polarization expressed in global coordinates can be expressed as:

$$E_x = E_X \cos(\beta) + E_Y \sin(\beta)$$

$$E_y = -E_X \sin(\beta) + E_Y \cos(\beta)$$

$$P_x = \chi_{xxx} E_x^2 - \chi_{xxx} E_y^2$$

$$P_y = -2\chi_{xxx} E_x E_y$$

$$P_X = P_x \cos(\beta) - P_y \sin(\beta)$$

$$P_Y = P_x \sin(\beta) + P_y \cos(\beta)$$

We take the off-resonant susceptibility value of MoS_2 to be 0.7 (10^4 pm^2/V) as reported. Results shown in Figure S14 are SHG polarization results of MoS_2 with a Y-orientated analyzer before

the detector from the spatial distribution of incident field using the Vector model (orange dots) and from a simple analytical model ($I(\omega) = C\chi_{xxx}^2 \cos(3\beta)^2 I(\omega)^2$) with uniform incident field (yellow line), respectively. The results from both models show excellent agreement except a constant multiplier and this is acceptable since MoS_2 will not react to incident E_z and all responses are confined to be in-plane.

Next, we use the Vector model developed above to simulate the SH response from tBLG. For overall SH intensity comparison between MoS_2 and tBLG, there is no polarizer before the detector and intensities are normalized by the signal from MoS_2. Plots in Figure S15 are the angle-dependent SH intensity from tBLG with different values of χ_{xyz}. χ_{xxx} is chosen to be 100 times smaller than χ_{xyz} based on DFT results. Although there is no analyzer, angle-dependent SH intensity reveals the interference between different nonlinear tensor components agrees with our experimental observations (Figure 3b-d).

For the SH intensity comparison in Figure 2c, both MoS_2 and 6° tBLG are excited by 1064nm CW laser and the collected maximum SH intensity are comparable. The excitation for MoS_2 is off-resonant with susceptibility around 0.7×10^4 pm^2/V. On the other hand, the excitation is resonant for 6° tBLG and as shown in Figure S15. Since the susceptibility of tBLG should be around 28×10^4 pm^2/V in order to achieve comparable values, the susceptibility for resonantly excited tBLG should be on the same order of resonantly excited TMDC system. The discrepancy of estimated values of tBLG susceptibility from a simple analytical model (3 (10^4 pm^2/V)) and from the Vector model (28 (10^4 pm^2/V)) not only uncovers the role of E_z enabled by the high-NA objective but also discloses the necessity of the Vector model to analyze the observed SH signal for our case.

G peak enhancement fitting:

The enhancement of Raman G peak of tBLGs can be described by second order time dependent perturbation[10]:

$$\frac{I_G}{I_{SLG}} = |\frac{M}{(E_{inc} - E_{vHs} - i\gamma)(E_{inc} - E_{vHs} - \hbar\omega_G - i\gamma)}|^2$$

In our case, E_{inc}(energy of incident photon) and $\hbar\omega_G$(energy of G phonon) is fixed and E_{vHs} is varied. By assuming M and γ are constant across all samples and using least square to fit the data in Figure 4a, we obtain the solid yellow curve in Figure 4a. We found $M = 0.3318 \pm 0.00867$ and $\gamma = 0.2002 \pm 0.345$ consistent with results obtained in Ref 10. The nice fitting results show that the above assumption is feasible.

SHG enhancement fitting:

SHG enhancement data in Figure 4b are fitted by a coherent superposition of second-order nonlinear susceptibility of 1ω and 2ω resonances[42, 43]:

$$I(2\omega) \propto (\chi^{(2)})^2 \propto (\frac{f_1 \exp(i\varphi_1)}{(E_{inc} - E_{vHs} + i\Gamma_1/2)} + \frac{f_2 \exp(i\varphi_2)}{(2E_{inc} - E_{vHs} + i\Gamma_2/2)})^2$$

where E_{inc} is the energy of incident light, E_{vHs} corresponds to the energy of vHs transitions in tBLG. In this work, we are using different twist angles to demonstrate the tunable nonlinear response of the tBLG system, therefore E_{inc} is fixed to be 1.58eV and E_{vHs} is swept from 0 to 4eV. The phase value φ_i does not play an important role here because the two resonant frequencies are well separated. f_i and Γ_i (i=1, 2) determines the amplitude and the bandwidth of resonant peaks respectively. The solid line in Figure 4b is the fitting result which shows that 1-photon resonance is around 1.573eV and 2-photon resonance is around 3.158eV in line with expectations.

ACKNOWLEDGEMENTS

This work is supported by Bakar Fellowship. Work at the Molecular Foundry was supported by the Office of Science, Office of Basic Energy Sciences, of the U.S. Department of Energy under Contract No. DE-AC02-05CH11231. W.S and L.Y. are supported by the Air Force Office of Scientific Research (AFOSR) grant No. FA9550-17-1-0304 and the National Science Foundation (NSF) CAREER Grant No. DMR-1455346. The computational resources have been provided by the Stampede of Teragrid at the Texas Advanced Computing Center (TACC) through XSEDE.

AUTHOR CONTRIBUTIONS

F.Y. and J.Y. conceived the project and designed the experiments. F.Y., F.M., F.L. and S.L. fabricated the tBLG samples. W.S. and L.Y. provided numerical calculations. F.Y., S.L., Z.G., J.C., E.B. and E.C contributed to optical characterizations. F.Y. and J.Y. wrote the paper with input from all authors.

DECLARARION OF INTERESTS

The authors declare no competing interests.

Figure 1 | Schematics of bilayer graphene and mapping results of tBLG. a AB-stacked bilayer graphene crystal structure with an additional translational replacement (T) and relative twist (R). The top and bottom layers are labeled as blue and red, respectively. **b** Bandstructure of a 21.8° tBLG. The red and blue arrows near M point indicate transitions between vHs in valance and conduction bands. **c** Schematics for 1- and 2- photon resonant SHG processes **d** Optical image of a tBLG with 8° twisted angle. The tBLG region, single-layer graphene region under hBN and pure single-layer graphene on substrate region are indicated by red, green and blue dashed boxes. The white box corresponds to the following mapping area. (**e** and **f**) Raman R peak mapping and SHG mapping of the 8° tBLG sample using 532nm and 1064nm CW laser respectively. Scale bar: 10um.

Figure 2 | Raman and SHG results of tBLG. a Raman spectra of 8° tBLG sample under hBN (black) and monolayer graphene (red) under 532nm excitation. **b** SHG power dependence of 8° tBLG sample in log-log scale. The dotted data (red) were fitted linearly with a slope of 1.97 ± 0.06 (a.u.). **c** SHG spectra of TLG (light blue), tBLG (dark blue) and CVD-grown monolayer MoS_2 (purple). The spectra are shifted vertically for a clearer view. The insert of **c** compares the relative amplitude of the SHG signal of three species under the same experimental configuration excited by 1064nm CW laser.

Figure 3 | SHG polarization pattern and calculated second-order susceptibility tensors. a-d SHG polarization pattern of an odd-layer hBN, 8°, 10°, and 12° tBLG samples respectively with a polarizer vertical to the polarization of incident laser before the detector. **e** and **f** DFT calculation of second-order susceptibility response in x and y direction of a 21.8° tBLG model.

Figure 4 | Change of Raman and SHG signal with twist angle. a Raman G peak enhancement with different twist angles using 532nm laser. The orange dots are experimental results and the yellow curve is the G peak enhancement fitting based on the work[10]. **b** Normalized SHG signal of tBLGs with different twist angles under 785nm excitation. The orange dots are experimental data and the yellow curve is the fitting result. The insets correspond to 1- and 2- photon resonant SHG processes. We used the highest count in the polarization plot of all tBLG samples for the figure. **c** Spectrum of the imaginary part of linear permittivity in z-direction (purple) and the absolute value of χ_{xyz} (blue) of a 21.8° tBLG.

REFERENCES:

1. Cao, Y., Fatemi, V., Demir, A., Fang, S., Tomarken, S.L., Luo, J.Y., Sanchez-Yamagishi, J.D., Watanabe, K., Taniguchi, T., Kaxiras, E., et al. (2018). Correlated insulator behaviour at half-filling in magic-angle graphene superlattices. Nature **556**, 80-84.
2. Cao, Y., Fatemi, V., Fang, S., Watanabe, K., Taniguchi, T., Kaxiras, E. & Jarillo-Herrero, P. (2018). Unconventional superconductivity in magic-angle graphene superlattices. Nature **556**, 43-50.
3. Yankowitz, M., Chen, S.W., Polshyn, H., Zhang, Y.X., Watanabe, K., Taniguchi, T., Graf, D., Young, A.F. & Dean, C.R. (2019). Tuning superconductivity in twisted bilayer graphene. Science **363**, 1059-1064.
4. Sharpe, A.L., Fox, E.J., Barnard, A.W., Finney, J., Watanabe, K., Taniguchi, T., Kastner, M.A. & Goldhaber-Gordon, D. (2019). Emergent ferromagnetism near three-quarters filling in twisted bilayer graphene. Science **365**, 605-608.
5. Zou, L.J., Po, H.C., Vishwanath, A. & Senthi, T. (2018). Band structure of twisted bilayer graphene: Emergent symmetries, commensurate approximants, and Wannier obstructions. Phys Rev B **98** 085435.
6. Havener, R.W., Liang, Y.F., Brown, L., Yang, L. & Park, J. (2014). Van Hove Singularities and Excitonic Effects in the Optical Conductivity of Twisted Bilayer Graphene. Nano Lett **14**, 3353-3357.
7. Li, G.H., Luican, A., dos Santos, J.M.B.L., Castro Neto, A.H., Reina, A., Kong, J. & Andrei, E.Y. (2010). Observation of Van Hove singularities in twisted graphene layers. Nat Phys **6**, 109-113.
8. Patel, H., Havener, R.W., Brown, L., Liang, Y.F., Yang, L., Park, J. & Graham, M.W. (2015). Tunable Optical Excitations in Twisted Bilayer Graphene Form Strongly Bound Excitons. Nano Lett **15**, 5932-5937.
9. Patel, H., Huang, L.J., Kim, C.J., Park, J. & Graham, M.W. (2019). Stacking angle-tunable photoluminescence from interlayer exciton states in twisted bilayer graphene. Nat Commun **10** 1445.
10. Carozo, V., Almeida, C.M., Fragneaud, B., Bede, P.M., Moutinho, M.V.O., Ribeiro-Soares, J., Andrade, N.F., Souza, A.G., Matos, M.J.S., Wang, B., et al. (2013). Resonance effects on the Raman spectra of graphene superlattices. Phys Rev B **88** 085401.
11. Kim, C.J., Sanchez-Castillo, A., Ziegler, Z., Ogawa, Y., Noguez, C. & Park, J. (2016). Chiral atomically thin films. Nature Nanotechnology **11**, 520-524.
12. Jorio, A., Kasperczyk, M., Clark, N., Neu, E., Maletinsky, P., Vijayaraghavan, A. & Novotny, L. (2014). Optical-Phonon Resonances with Saddle-Point Excitons in Twisted-Bilayer Graphene. Nano Lett **14**, 5687-5692.
13. Yin, X.B., Ye, Z.L., Chenet, D.A., Ye, Y., O'Brien, K., Hone, J.C. & Zhang, X. (2014). Edge Nonlinear Optics on a MoS2 Atomic Monolayer. Science **344**, 488-490.
14. Li, Y.L., Rao, Y., Mak, K.F., You, Y.M., Wang, S.Y., Dean, C.R. & Heinz, T.F. (2013). Probing Symmetry Properties of Few-Layer MoS2 and h-BN by Optical Second-Harmonic Generation. Nano Lett **13**, 3329-3333.
15. Shan, Y.W., Li, Y.G., Huang, D., Tong, Q.J., Yao, W., Liu, W.T. & Wu, S.W. (2018). Stacking symmetry governed second harmonic generation in graphene trilayers. Sci Adv **4** eatt0074.
16. Dean, J.J. & van Driel, H.M. (2009). Second harmonic generation from graphene and

graphitic films. Appl Phys Lett **95** 261910.
17. Brun, S.J. & Pedersen, T.G. (2015). Intense and tunable second-harmonic generation in biased bilayer graphene. Phys Rev B **91** 205405.
18. Avetissian, H.K., Mkrtchian, G.F., Batrakov, K.G., Maksimenko, S.A. & Hoffmann, A. (2013). Multiphoton resonant excitations and high-harmonic generation in bilayer graphene. Phys Rev B **88** 165411.
19. Wu, S.F., Mao, L., Jones, A.M., Yao, W., Zhang, C.W. & Xu, X.D. (2012). Quantum-Enhanced Tunable Second-Order Optical Nonlinearity in Bilayer Graphene. Nano Lett **12**, 2032-2036.
20. Boyd, R.W. (2008). Nonlinear.Optics, 3rd Edition (Academic Press).
21. Hsu, W.T., Zhao, Z.A., Li, L.J., Chen, C.H., Chiu, M.H., Chang, P.S., Chou, Y.C. & Chang, W.H. (2014). Second Harmonic Generation from Artificially Stacked Transition Metal Dichalcogenide Twisted Bilayers. Acs Nano **8**, 2951-2958.
22. Psilodimitrakopoulos, S., Mouchliadis, L., Paradisanos, I., Kourmoulakis, G., Lemonis, A., Kioseoglou, G. & Stratakis, E. (2019). Twist Angle mapping in layered WS2 by Polarization-Resolved Second Harmonic Generation. Sci Rep **9** 14285.
23. Pizzocchero, F., Gammelgaard, L., Jessen, B.S., Caridad, J.M., Wang, L., Hone, J., Boggild, P. & Booth, T.J. (2016). The hot pick-up technique for batch assembly of van der Waals heterostructures. Nat Commun **7** 11894.
24. Wang, X.H., Chang, S.J., Lin, L., Wang, L.R., Huo, B.Z. & Hao, S.J. (2010). Vector model for polarized second-harmonic generation microscopy under high numerical aperture. J Optics **12** 045201.
25. Malard, L.M., Alencar, T.V., Barboza, A.P.M., Mak, K.F. & de Paula, A.M. (2013). Observation of intense second harmonic generation from MoS2 atomic crystals. Phys Rev B **87** 201401.
26. Trolle, M.L., Seifert, G. & Pedersen, T.G. (2014). Theory of excitonic second-harmonic generation in monolayer MoS2. Phys Rev B **89** 235410.
27. Lui, C.H., Mak, K.F., Shan, J. & Heinz, T.F. (2010). Ultrafast Photoluminescence from Graphene. Phys Rev Lett **105** 127404.
28. Liu, W.T., Wu, S.W., Schuck, P.J., Salmeron, M., Shen, Y.R. & Wang, F. (2010). Nonlinear broadband photoluminescence of graphene induced by femtosecond laser irradiation. Phys Rev B **82** 081408.
29. Alencar, T.V., von Dreifus, D., Moreira, M.G.C., Eliel, G.S.N., Yeh, C.H., Chiu, P.W., Pimenta, M.A., Malard, L.M. & de Paula, A.M. (2018). Twisted bilayer graphene photoluminescence emission peaks at van Hove singularities. J Phys Condens Mat **30** 175302.
30. Koshino, M. & Moon, P. (2015). Electronic Properties of Incommensurate Atomic Layers. J Phys Soc Jpn **84** 121001.
31. Verbiest, T., Van Elshocht, S., Kauranen, M., Hellemans, L., Snauwaert, J., Nuckolls, C., Katz, T.J. & Persoons, A. (1998). Strong enhancement of nonlinear optical properties through supramolecular chirality. Science **282**, 913-915.
32. Verbiest, T., Van Elshocht, S., Persoons, A., Nuckolls, C., Phillips, K.E. & Katz, T.J. (2001). Second-order nonlinear optical properties of highly symmetric chiral thin films. Langmuir **17**, 4685-4687.
33. Dailey, C.A., Burke, B.J. & Simpson, G.J. (2004). The general failure of Kleinman symmetry in practical nonlinear optical applications. Chem Phys Lett **390**, 8-13.

34. Song, W.S., Guo, G.Y., Huang, S., Yang, L. & Yang, L. (2020). First-principles Studies of Second-Order Nonlinear Optical Properties of Organic-Inorganic Hybrid Halide Perovskites. Phys Rev Appl **13** 014052.
35. Kang, H., Jia, B.H. & Gu, M. (2010). Polarization characterization in the focal volume of high numerical aperture objectives. Opt Express **18**, 10813-10821.
36. Yew, E.Y.S. & Sheppard, C.J.R. (2006). Effects of axial field components on second harmonic generation microscopy. Opt Express **14**, 1167-1174.
37. Wang, G., Robert, C., Glazov, M.M., Cadiz, F., Courtade, E., Amand, T., Lagarde, D., Taniguchi, T., Watanabe, K., Urbaszek, B., et al. (2017). In-Plane Propagation of Light in Transition Metal Dichalcogenide Monolayers: Optical Selection Rules. Phys Rev Lett **119** 047401.
38. Sato, K., Saito, R., Cong, C.X., Yu, T. & Dresselhaus, M.S. (2012). Zone folding effect in Raman G-band intensity of twisted bilayer graphene. Phys Rev B **86** 125414.
39. Eliel, G.S.N., Moutinho, M.V.O., Gadelha, A.C., Righi, A., Campos, L.C., Ribeiro, H.B., Chiu, P.W., Watanabe, K., Taniguchi, T., Puech, P., et al. (2018). Intralayer and interlayer electron-phonon interactions in twisted graphene heterostructures. Nat Commun **9** 1221.
40. Patankar, S., Wu, L., Lu, B.Z., Rai, M., Tran, J.D., Morimoto, T., Parker, D.E., Grushin, A.G., Nair, N.L., Analytis, J.G., et al. (2018). Resonance-enhanced optical nonlinearity in the Weyl semimetal TaAs. Phys Rev B **98** 165113.
41. Wang, G., Marie, X., Gerber, I., Amand, T., Lagarde, D., Bouet, L., Vidal, M., Balocchi, A. & Urbaszek, B. (2015). Giant Enhancement of the Optical Second-Harmonic Emission of WSe2 Monolayers by Laser Excitation at Exciton Resonances. Phys Rev Lett **114** 097403.
42. Erley, G., Daum, W. (1998). Silicon interband transitions observed at Si(100)-SiO_2 interfaces. Phys Rev B **58** R1734(R).
43. Takanori, S. (2000). Surface-state transitions of Si(111)-7x7 probed using nonlinear optical spectroscopy. Phys Rev B **61** R5117(R).
44. Liu, Y., Wang, J., Kim, S., Sun, H.Y., Yang, F.Y., Fang, Z.X., Tamura, N., Zhang, R.P., Song, X.H., Wen, J.G., et al. (2019). Helical van der Waals crystals with discretized Eshelby twist. Nature **570**, 358-362.
45. Shallcross, S., Sharma, S., Kandelaki, E. & Pankratov, O.A. (2010). Electronic structure of turbostratic graphene. Phys Rev B **81** 165105.
46. Kresse, G. & Furthmuller, J. (1996). Efficient iterative schemes for ab initio total-energy calculations using a plane-wave basis set. Phys Rev B **54**, 11169-11186.
47. Kresse, G. & Joubert, D. (1999). From ultrasoft pseudopotentials to the projector augmented-wave method. Phys Rev B **59**, 1758-1775.
48. Perdew, J.P., Burke, K. & Ernzerhof, M. (1996). Generalized gradient approximation made simple. Phys Rev Lett **77**, 3865-3868.
49. Grimme, S. (2006). Semiempirical GGA-type density functional constructed with a long-range dispersion correction. J Comput Chem **27**, 1787-1799.
50. Taghinejad, M., Xu, Z.H., Wang, H., Taghinejad, H., Lee, K.T., Rodrigues, S.P., Adibi, A., Qian, X.F., Lian, T.Q., Cai, W.S. (2020). Photocarrier-induced active control of second-order optical nonlinearity in Monolayer MoS_2. Small **16**, 1906347.
51. Mannebach, E.M., Duerloo, K.A.N., Pellouchoud, L.A., Sher, M.J., Nah, S.H., Kuo, Y.H., Yu, Y.F., Marshall, A.F., Cao, L.Y., Reed, E.J., Lindenberg, A.M. (2014). Ultrafast electronic and structural response of Monolayer MoS_2 under intense photoexcitation

conditions. ACS Nano , 10735-10742.
52. Jang, H., Dhakal, K.P., Joo, K.I., Yun, W.S., Shinde, S.M., Chen, X., Jeong, S.M., Lee, S.W., Lee, Z.H., Lee, J.D., Ahn, J.H., Kim, H.M. (2018). Transient SHG imaging on Ultrafast Carrier Dynamics of MoS_2 Nanosheets. Adv Mater **30**, 1705190.

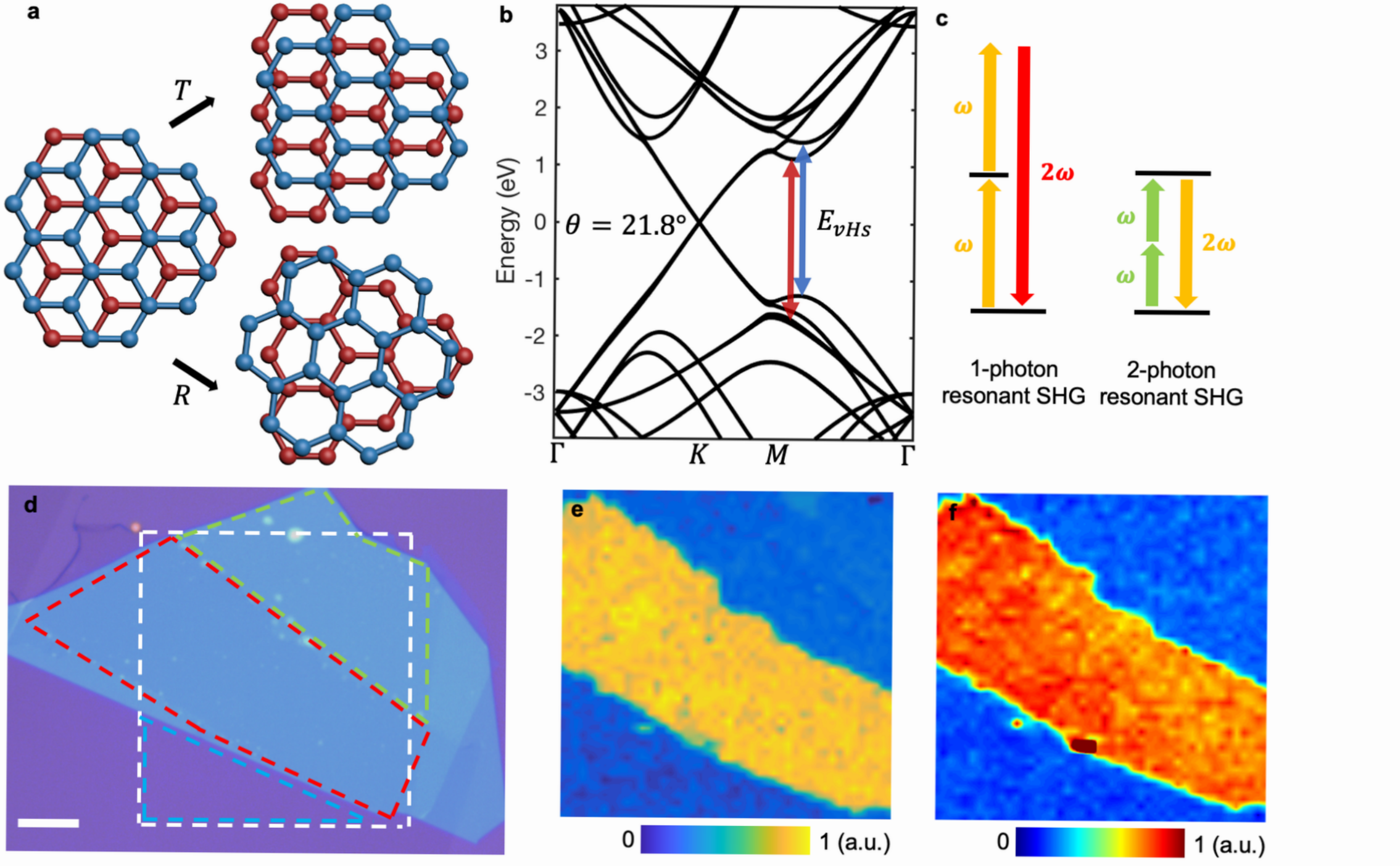
a
T
R
b
Energy (eV)
3
2
1
0
-1
-2
-3
θ = 21.8°
E_vHs
Γ
K
M
Γ
c
ω
ω
2ω
1-photon resonant SHG
ω
ω
2ω
2-photon resonant SHG
d
e
0
1 (a.u.)
f
0
1 (a.u.)

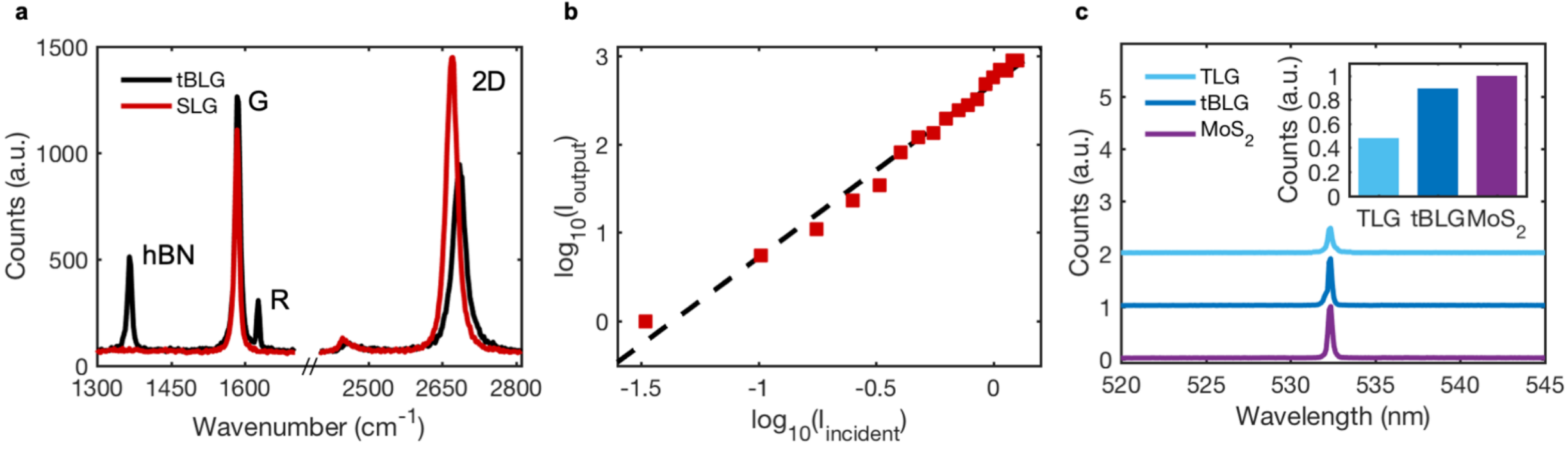
a
tBLG
SLG
G
2D
hBN
R
Counts (a.u.)
Wavenumber (cm^{-1})
b
$\log_{10}(I_{output})$
$\log_{10}(I_{incident})$
c
TLG
tBLG
MoS_2
Counts (a.u.)
Wavelength (nm)

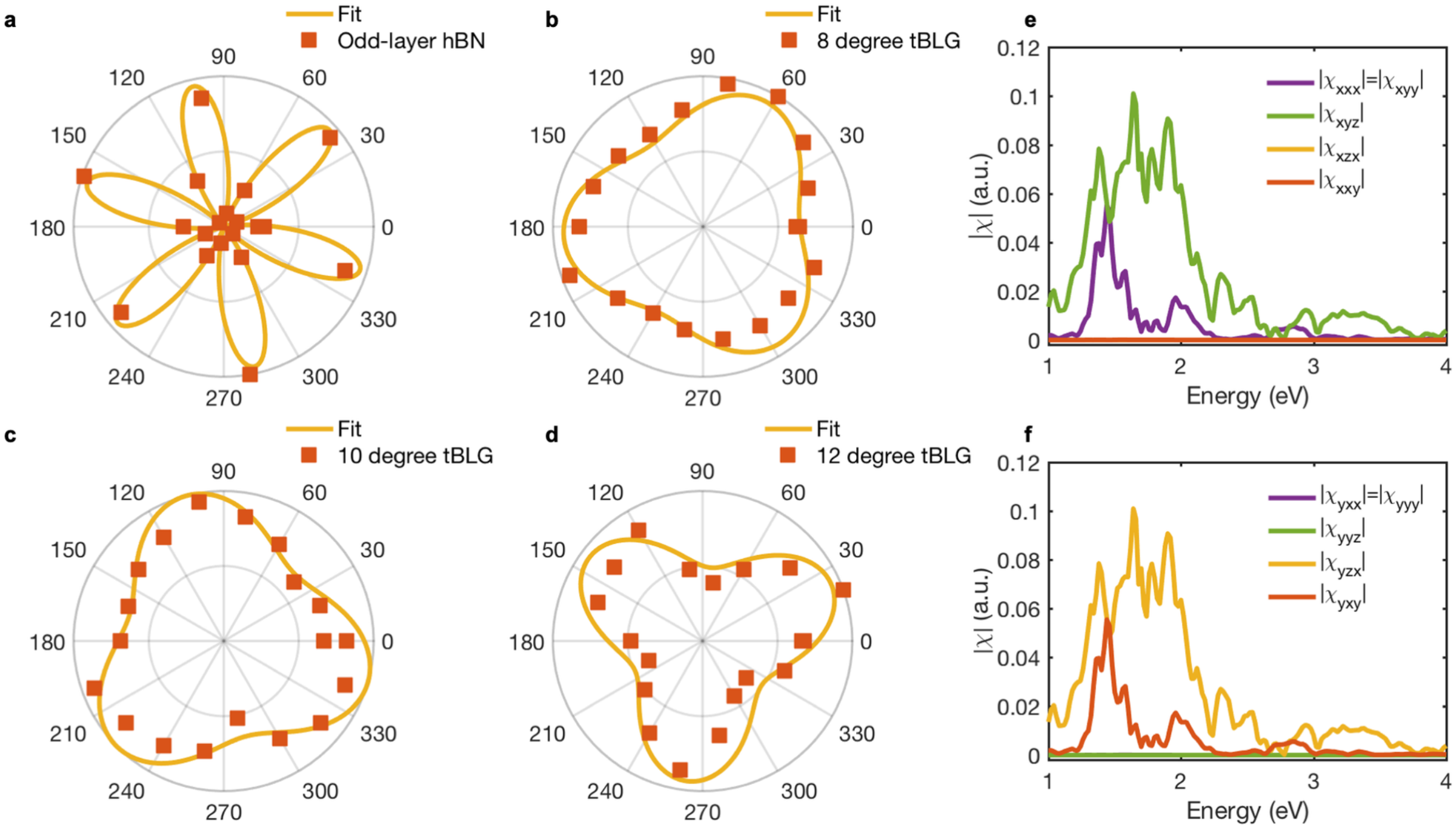
a
Fit
Odd-layer hBN
b
Fit
8 degree tBLG
c
Fit
10 degree tBLG
d
Fit
12 degree tBLG
90
60
30
0
330
300
270
240
210
180
150
120
e
f
|χ| (a.u.)
Energy (eV)
0
0.02
0.04
0.06
0.08
0.1
0.12
1
2
3
4
|χxxx|=|χxyy|
|χxyz|
|χxzx|
|χxxy|
|χyxx|=|χyyy|
|χyyz|
|χyzx|
|χyxy|

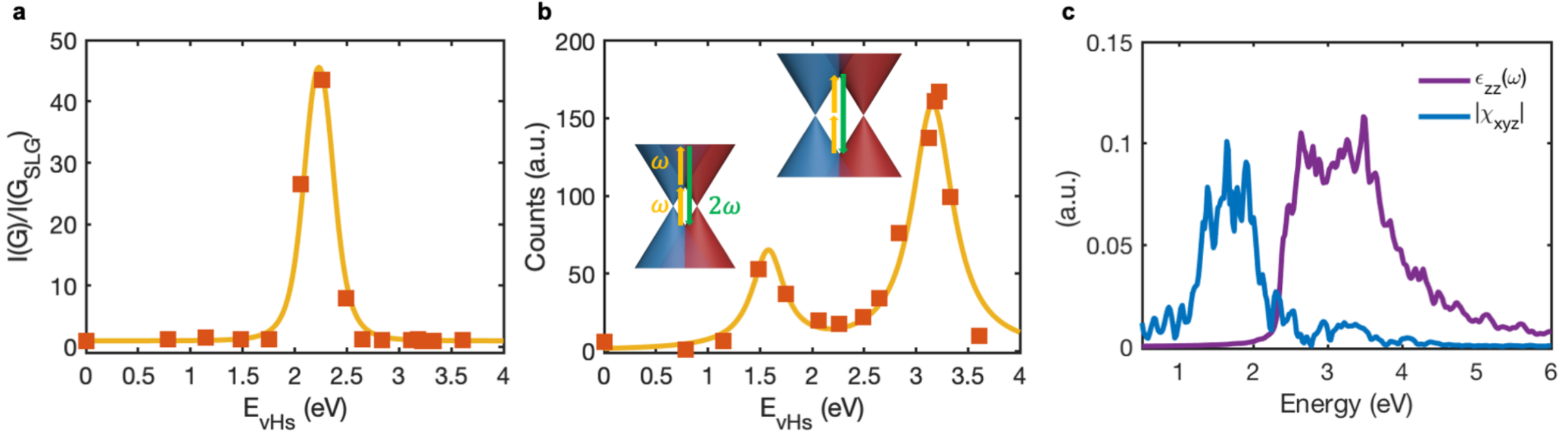
a
I(G)/I(G_SLG)
E_vHs (eV)
b
Counts (a.u.)
E_vHs (eV)
ω
ω
2ω
c
(a.u.)
Energy (eV)
ϵ_zz(ω)
|χ_xyz|

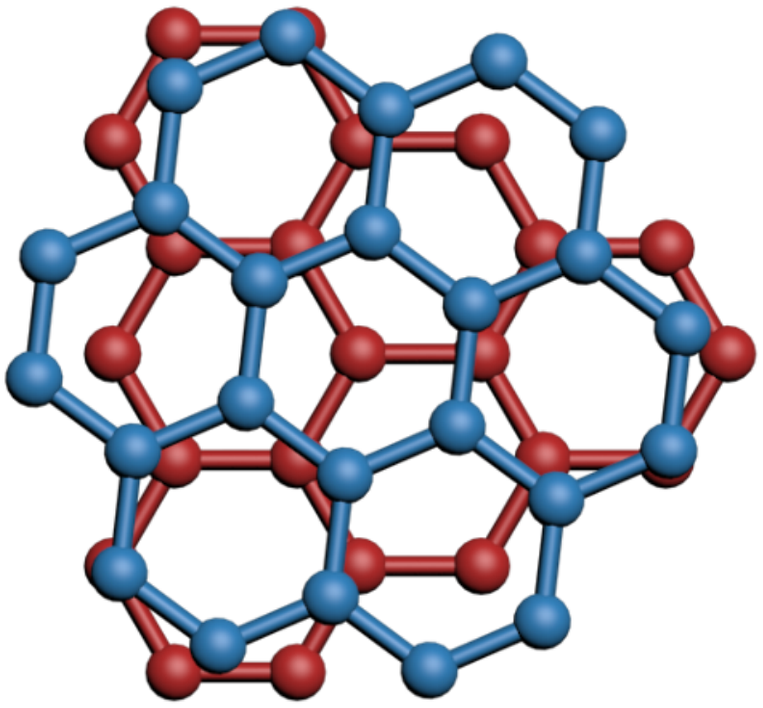

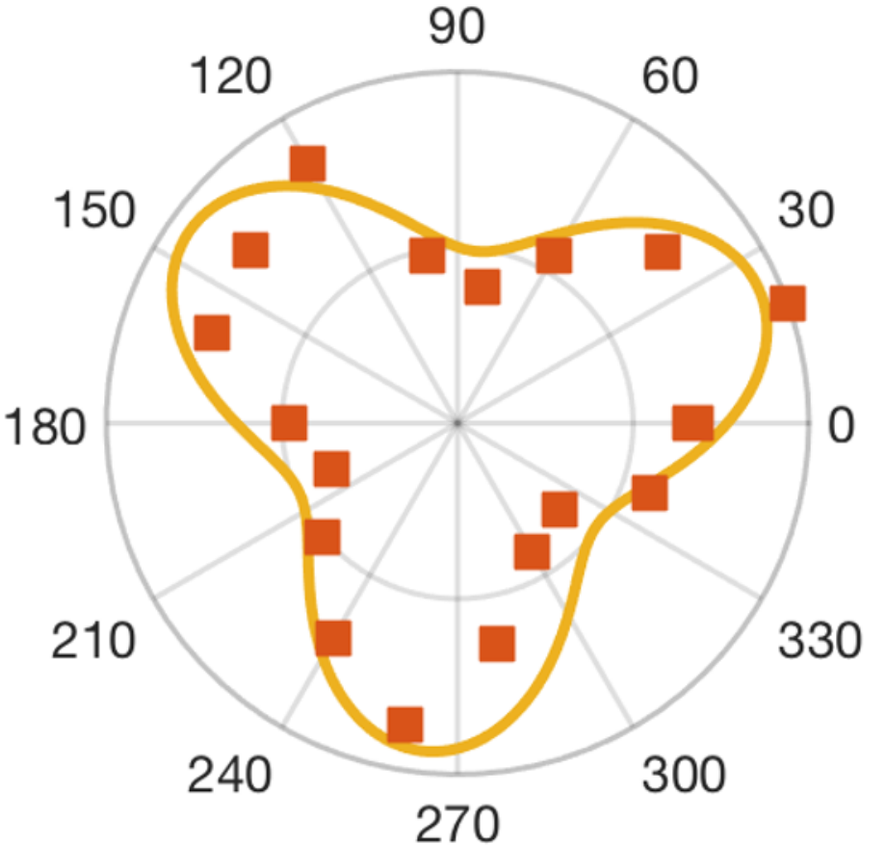
90
120
60
150
30
180
0
210
330
240
300
270

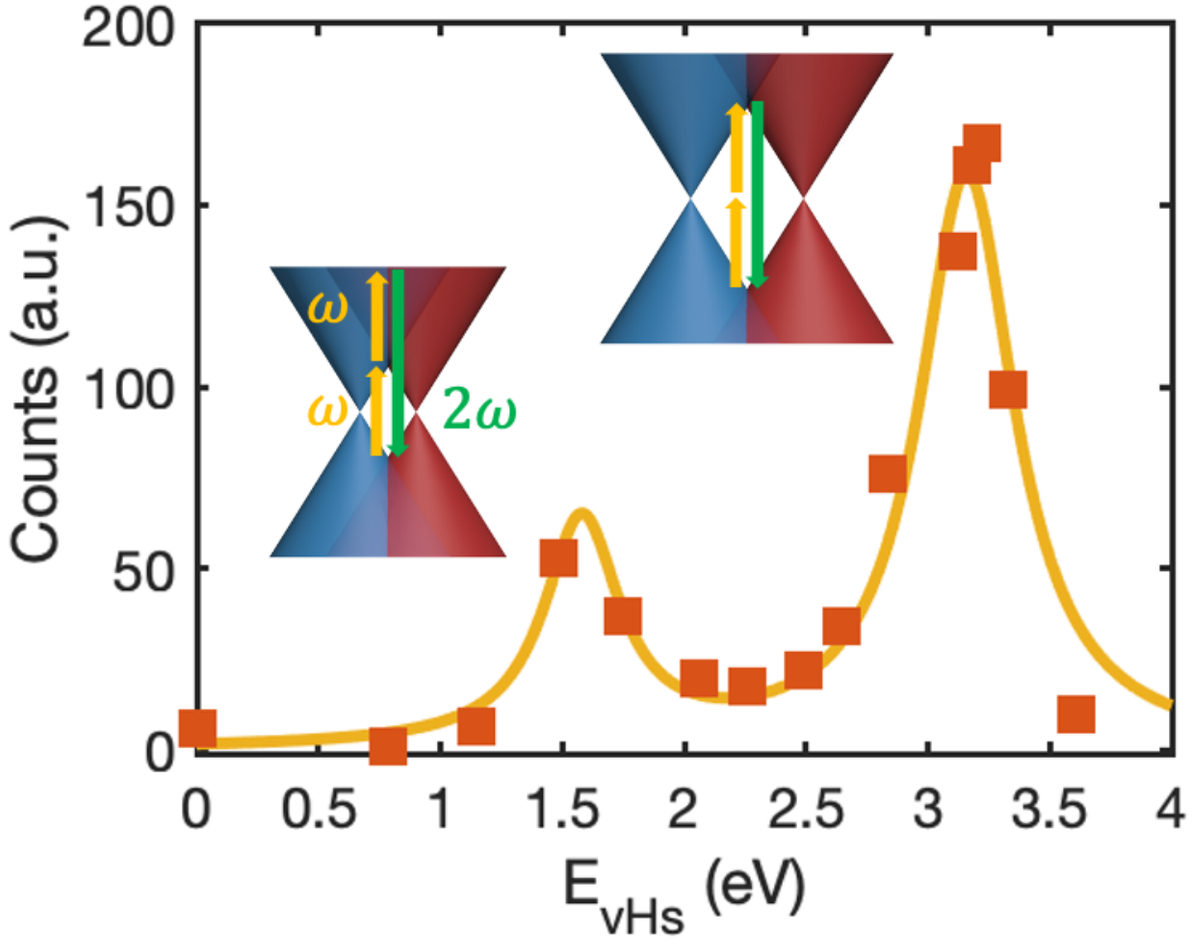
200
150
100
50
0
Counts (a.u.)
0
0.5
1
1.5
2
2.5
3
3.5
4
E vHs (eV)
ω
ω
2ω